Journal of MATERIALS RESEARCH

Article
DOI:10.1557/s43578-022-00773-1

# Synthesis of composite graphitic scaffolds using polysaccharide precursors

Fabian Villalobos[1], Andrew Patalano[2], Steven Herrera[1], Ryan Wu[3], Daisy Patino[1], Pedro A. Peña[2], Evan Jauregui[4], Amir-Ali Akhavi[1], William Coley[1], Andre Mkhoyan[3], Mihrimah Ozkan[1,2,5,a)], Cengiz S. Ozkan[1,2,6,a)]

[1] Materials Science and Engineering Program, University of California, Riverside, CA 92521, USA
[2] Department of Chemistry, University of California, Riverside, CA 92521, USA
[3] Department of Chemical Engineering and Materials Science, University of Minnesota, Minneapolis, MN 55455-0132, USA
[4] Department of Chemical and Environmental Engineering, University of California, Riverside, CA 92521, USA
[5] Department of Electrical and Computer Engineering, University of California, Riverside, CA 92521, USA
[6] Department of Mechanical Engineering, University of California, Riverside, CA 92521, USA
[a)] Address all correspondence to these authors. e-mails: mihri@ece.ucr.edu; cozkan@engr.ucr.edu

Received: 28 July 2022; accepted: 29 September 2022; published online: 24 October 2022

**We describe a method for synthesizing porous carbon scaffolds embedded with metal particles. An analysis of the growth mechanism by esterification of polysaccharides at low pH is conducted. Iron-nitrate precursors nucleate iron particles via oxidative process when annealed under a reducing atmosphere and embedded within a porous carbon matrix. The process was then applied to other metal nitrates (Co, Ni, Cu, Ag, and Al). Co and Ni nanoparticles exhibited an encapsulating graphitic layer while Cu, Ag, and Al nanoparticles did not. A potential mechanism by which graphitic encapsulation takes place in Fe, Co, and Ni is suggested by comparison to phase separation during the growth of carbon nanotubes from catalytic metal nanoparticles. This flexible method for synthesizing composite porous carbon scaffolds with metal nanoparticles is achievable using cheap, environmentally benign precursors which can be employed in future applications toward capacitors, oil sorption, spill recovery, and bactericidal coatings.**

## Introduction

Porous carbon materials have applications ranging from electrochemical electrode materials [1–7] to filtration of oils and non-polar solvents [6, 8–14] due to properties such as conductivity and large surface area. In the past few years of developing these porous materials, researchers have moved away from using tar pitches and have placed emphasis on using environmentally benign precursors that can decompose in nature without fear of unforeseen repercussions. For this reason, natural polymers and carbohydrates such as cellulose, starch, and chitin have been investigated as potential precursors for these porous carbon materials [15–17].These porous carbon structures can be referred to in literature as foams and sponges. Sucrose in particular has been used as a precursor in many such studies to synthesize a porous bulk morphology to increase surface area [2, 8, 18, 19].

In this work we seek to expand upon the potential applications of porous carbon materials synthesized from polysaccharides. The properties afforded by the embedded nanoparticles serve to make these porous materials. With the porous carbon network acting as a high surface area scaffold for the metal, the nanoparticles catalyze reactions such as the growth of carbon nanotubes [8]. Metals such as Fe, Co, and Ni nanoparticles are ferromagnetic which is helpful in retrieval of sorbents in solution such retrieving an oil soaked sorbent from a water–oil mixture. Antibacterial and bactericidal properties of Ag and Cu nanoparticles [20–23] could potentially be impregnated into high surface area carbon structures allowing for simultaneous sorption and bactericide. These porous composite materials are referred to as metal carbon foams (MCFs) in this work.

This work seeks to further elucidate and optimize the material's synthesis process via understanding of its chemical

and crystallization mechanisms. Previous works have demonstrated the synthesis of graphite encapsulated Fe nanoparticles embedded within a porous carbon matrix which displayed oleophilic, hydrophobic, and ferromagnetic properties [8, 24–26]. Without this, improvement of the material's properties and fabrication methods cannot be proposed. For this reason, the scope of this study was to identify the mechanisms responsible for the growth of the porous bulk morphology, nucleation of iron nanoparticles, and graphite encapsulation of said iron nanoparticles. Using the insights into the growth mechanism of oxidized polysaccharides annealed to produce composite materials comprised a porous, amorphous carbon matrix embedded with metal particles, new foam variants were fabricated by substituting several metal nitrate precursors thereby enabling the tailoring of these porous materials for future applications.

## Results and discussion

### Growth of porous carbon morphology

#### Oxidation of glucose

The oxidation of polysaccharides by nitric acid is well documented in literature [27–30]. Sucrose is a heterooligosaccharide, meaning it produces an equimolar mixture of D-glucose and D-fructose upon hydrolysis. During mixing in aqueous solution, proton transfer between $H_2O$ and the metal nitrate forms nitric acid, and at sufficiently low pH, can form $NO_2$ [31, 32], while the iron cation may undergo further hydrolysis reactions in solution[28, 31, 33]. A review of carbohydrate chemistry suggests that when glucose is hydrolyzed, the monosaccharide is free to mutarotate and the isomerization between the $\alpha$ and $\beta$ orientation of the primary alcohol produces a transitory acyclic glucose with the hemiacetal group forming an aldehyde at C1 and terminal alcohol at C6 as seen in Fig. 1. In aqueous solution, the C1 aldehyde group can undergo hydrolysis to form a geminal diol intermediate. Nitric acid could then form a protonated nitrate ester which then decomposes into a deprotonated nitrate ester and hydronium ion. Upon rearrangement, the nitrite ester produces a carboxylic acid at C1 and a nitrous acid molecule ($HNO_2$). This is the gluconic acid structure. Next, $HNO_2$ can oxidize the C6 terminal alcohol in the gluconic acid by nucleophilic attack at the nitrite forming another nitrite intermediate. This could decompose into a nitrite ester and produce a hydronium ion in aqueous solution. Rearrangement of the nitrite ester then produces a C6 aldehyde and nitroxyl molecule (HNO) [31]. Further oxidation of the C6 aldehyde by nitrate can proceed as discussed earlier, producing the saccharic or glucaric acid structure. The C1 aldehyde is more likely to oxidize before the C6 alcohol due to better electrophilic attraction. Simple esterification between saccharic acids polymerizes and produces the gelatinous resin.

A control experiment to confirm sugar oxidation was performed, excluding the metal cations and PVA and treated each of the following with nitric acid: sucrose, glucose, fructose, and gluconic acid. Each control was treated to pH 1, heated to the requisite 120 °C, cured, and annealed per the procedure highlighted above. Each control produced a gelatinous resin which expanded upon curing. This provides evidence that PVA is not required for the polymerization of sugars, or the bulk morphology, and that the oxidized products can and do polymerize with each other. Still, gluconic acid and saccharic acid may form linkages with PVA by simple esterification between the carboxylic acid and alcohol groups, respectively; experiments designed to elucidate this esterification mechanism were conducted using adipic acid, a 6-carbon organic compound with terminating carboxylic acids lacking alcohol groups.

Experiments treating adipic acid with nitric acid to pH 1 did not result in gelled resins. Additional polysaccharides (lactose, maltose, starch), hexoses (galactose) and pentoses (xylose, arabinose) as well as mucic acid were successful as foam precursors, especially when metal cations are included. Less successful precursors included malic acid and tartaric acid, 4 carbon organic compounds with terminating carboxylic acids and including alcohol groups. These two precursors were observed to produce small amounts of gel, but did not exhibit volumetric expansion or porous networks. Differences in the availability of alcohol groups compared to hexoses and pentoses may contribute to lack of volumetric expansion. These experiments provide evidence that oxidation of saccharides leads to esterification with

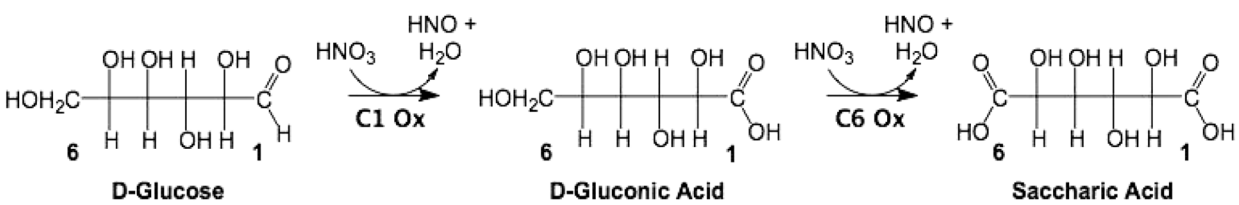


**Figure 1:** Oxidation of Glucose: Acyclic glucose in an acidic environment being oxidized to the gluconic acid intermediate, and further oxidized to saccharic acid, otherwise known as glucaric acid.

alcohol groups in other oxidized saccharides and possibly in PVA. All metal variations presented below use sucrose as the polysaccharide unless otherwise stated.

### Volumetric expansion and bulk morphology

During curing, the gelatinous resin is placed inside a vacuum oven, at around 250 torr and 150 °C. Water, nitrates, and $NO_x$ compounds evaporate in this temperature and pressure range. Any hydrogen bonding the resulting polymeric network exhibits can constrict the volume of the resin. The loss of water vapor nullifies existing hydrogen bonds and thereby increases the volume of void spaces in the gelatinous polymer-resin. Gaseous nitrogen and carbon compounds escaping the polymeric network leave behind void space that can increase surface area in a mechanism referred to as blowing [2, 6, 34, 35]. A comparison of the cell macrostructure for each of the synthesized MCFs is displayed in Fig. 2. The porosity is consistent between the metals chosen and structurally, the cells are of similar architecture; large outer "web-like" ligament structures with smaller, possibly mesoporous, cavities decorating the inner walls and connecting cells which is consistent with carbon foams in literature [6].

Microcomputed tomography (micro-CT) was performed on the Ni-xylose variant and CTVox software was used to isolate carbon (green) and higher-density metals in red as seen in the 272 µm × 176 µm × 48 µm section depicted in Fig. 3. The bulk of the foam architecture is composed of carbon while metal particles are distributed throughout the carbon structure. However, large concentrations of metals agglomerate at the joints and ligaments as seen in Fig. 3(c). This may be due to formation of the joints and ligaments during blowing. When in solution, the metal cations are thought to be mixed homogeneously, but as the polymerization takes place, bubbles form due to release of decomposition gases. The bubbles elongate the polymer-resin to create cell walls or ligaments as well as simultaneous contraction

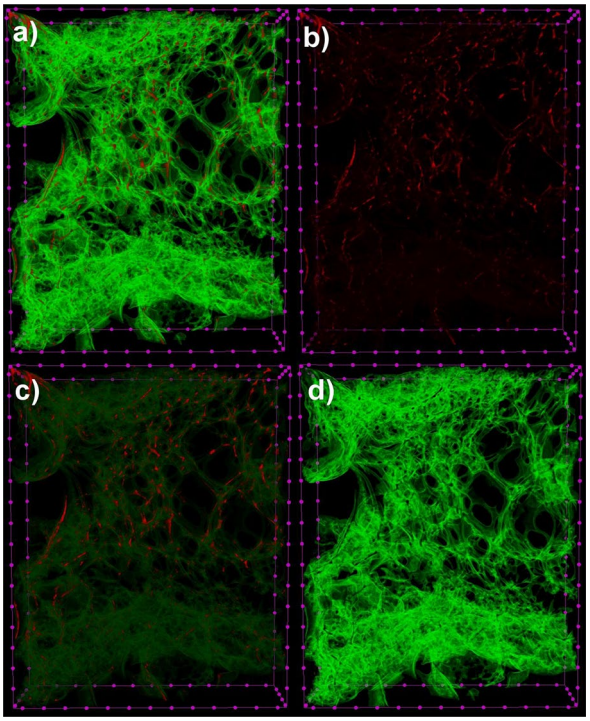


**Figure 3:** Micro-CT scans performed on the Nickel-Xylose foam variant which depicts (a) carbon and metal, (b) high-density signal showing metal particle distribution, (c) a combined mid-density and high-density signal with mid-density decreased to show overlay of red metal particle absorption, (d) mid-density carbon matrix. Each reference dot is spaced 16 µm apart.

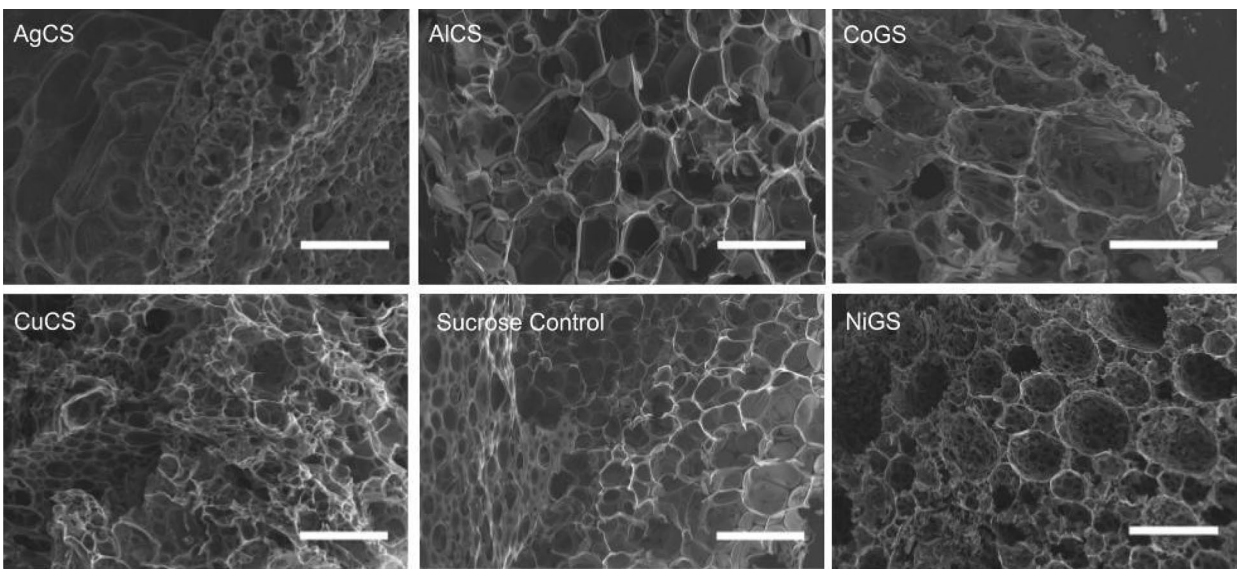


**Figure 2:** SEM micrographs of each of the new foam variants' porous macrostructures are depicted at 500 µm including the sucrose control.

into joints, each of which are embedded with the metals or metal salts. The concentration of the resultant polymer-resin into joints forces embedded metals into agglomeration at those areas during annealing.

Micro-CT scans were also performed on a Cu-lactose variant which is pictured in Fig. 4. Using Amira software, a reconstruction of the foam using the micro-CT scan was segmented into 3 volumes of differing density: the low-density volumes approximating the air and void space within the porous network as shown in Fig. 4(a), mid-density volumes showing a connected carbon network shown in Fig. 4(b), and high-density volumes approximating the metal particles as seen in Fig. 4(c). In the reconstruction, each colorized volume represents a volume which is not physically connected any other volume shown. For example: In Fig. 4(a), the light blue volume signifies a completely connected volume, which demonstrates that this is an open cell foam. In Fig. 4(b), the mid-density volume in dark blue displays the carbon structure as interconnected, with very little carbon separate from the main volume in dark blue. Figure 4(c) displays many separately colored high-density volumes, suggesting that metal particles are not highly interconnected and are instead dispersed throughout that foam's structure. The larger volumes in Fig. 4(c) are not considered as large particles. Due to the micro-CT's limits in resolution (0.351 µm voxel size), agglomerations of particles, as seen in the SEM micrograph Fig. 4(d), are detected as a single large volume. Volume percentage of each density segment was calculated to be: 73.68% low-density air and void space, 26.11% mid-density carbon, and 0.20% high-density copper metal. Assuming mid-density mass is carbon and high-density mass is copper, mass percentage was calculated to be 97.07% carbon and 2.92% copper. EDS of Cu-lactose sample records 85.58 mass% carbon, 10.76 mass% copper, and 3.68 mass% oxygen. Differences in the mass and weight between the two methods may be due to the limited resolution of micro-CT scans.

## Metal particles and graphite encapsulation

### Growth of metal particles

Three mechanisms are suggested for the growth of metal particles: First, during the mixing step, polysaccharide and

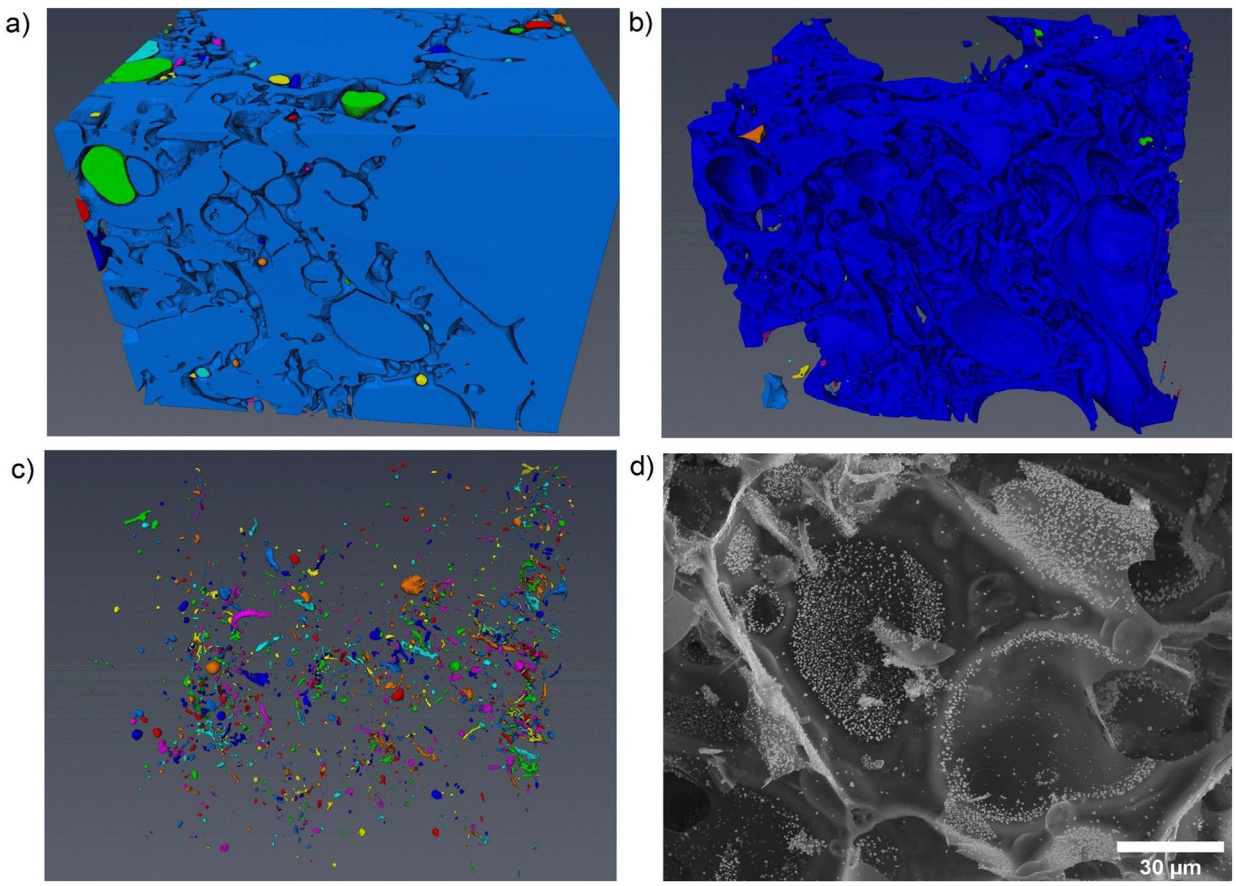


**Figure 4:** Micro-CT scans performed on the Cu-lactose variant where each color signifies a volume that is not physically connected to any other volume. Reconstruction of Cu-lactose foam depicts (a) volumes of low-density air and void space, (b) volumes of mid-density showing porous carbon structures, (c) high-density signal displaying volumes of metal particles d) SEM micrograph of Cu-lactose showing agglomerations of particles lining the struts, joints, and cell walls.

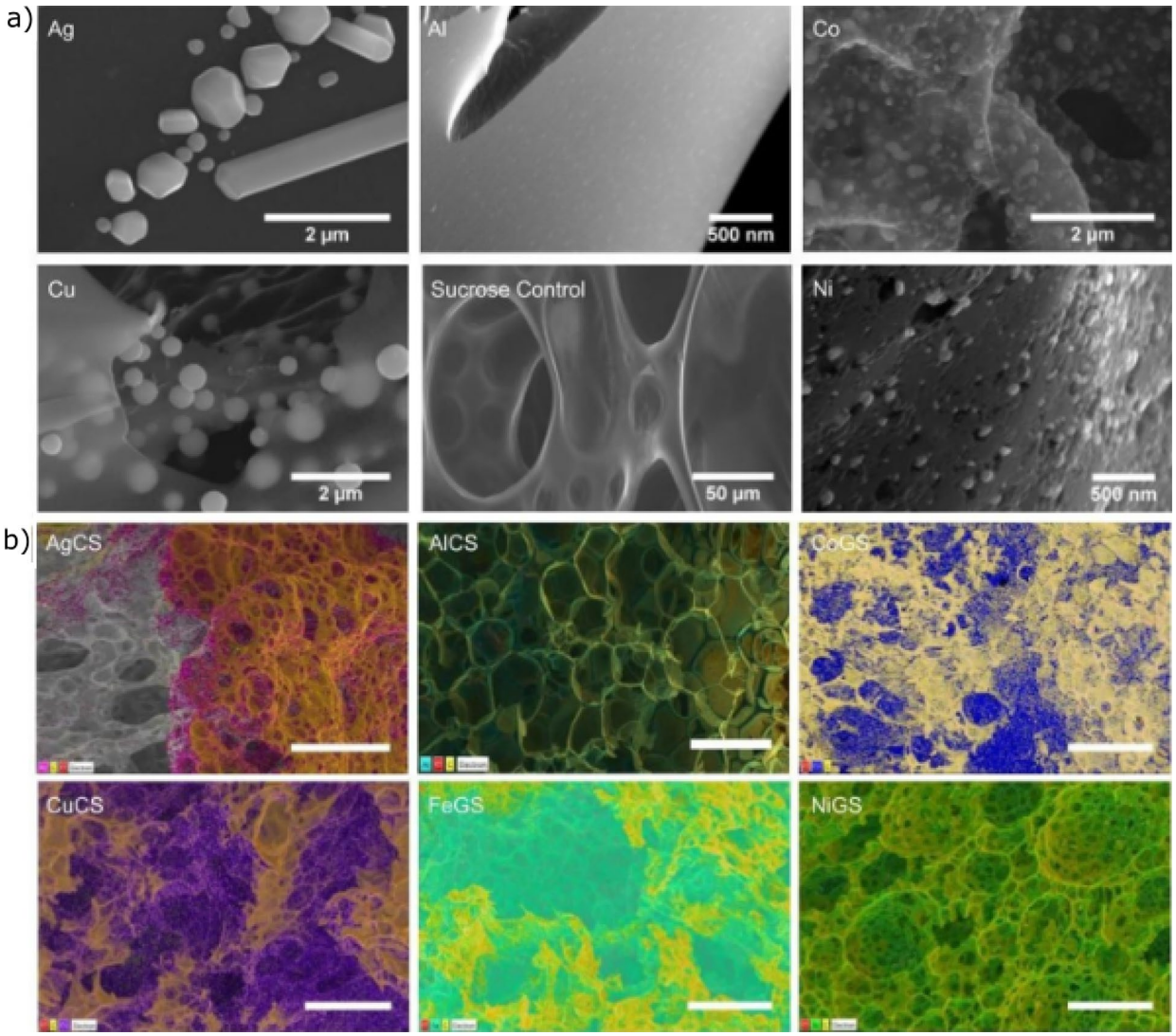


**Figure 5:** (a) Comparison of particles generated from respective metal nitrates chosen. Sucrose control sample did not exhibit any metal particles. (b) EDS Mapping of porous structures at 500 µm shows the distribution of embedded metal particles synthesized from the corresponding metal nitrate precursor. A partial map of the AgCF was acquired due to the depth of field of the structure.

metal nitrate precursors undergo hydrolysis reactions in aqueous solution. Metal cations are known to dissociate in aqueous environments and form aquo, hydroxyl, and oxo ligands depending on the pH of the solution [33]. These metal-ligands can then precipitate metal oxides in solution upon heating or increasing pH [33]. Nitrates and nitrites are present in solution during the mixing and oxidation of glucose, which may be catalyzed by the presence of metal cations, though further studies are needed to confirm. After curing at 150 °C under vacuum nitrate groups may still be present in the gelatinous resin. During annealing it is possible that nitrogen compounds form metal oxides as well [36], but in small, amorphous quantities that are not detectable by XRD; no crystallinity was detected in our characterization of the gelatinous resin. While exposing gelatinous resin to a reducing environment, $H_2$ gas removes oxygen through reduction, leaving reduced metal atoms that may nucleate into particles. However, the mixing of precursors in this study occurs at low pH, and the cations are therefore less prone to oxo ligand formation and metal oxide particles. Furthermore, a control experiment performed without the flow of $H_2$ gas, eliminating a reducing atmosphere, during the annealing step showed no presence of metal oxides detected by XRD for Fe carbon foam. The second suggested mechanism of metal particle growth is the reduction of metal cations by the sugars themselves. Silver and cupric ions are mild oxidants that oxidize reducing sugars like maltose, cellobiose, and lactose [20, 37, 38]. This would allow elemental metal atoms to nucleate

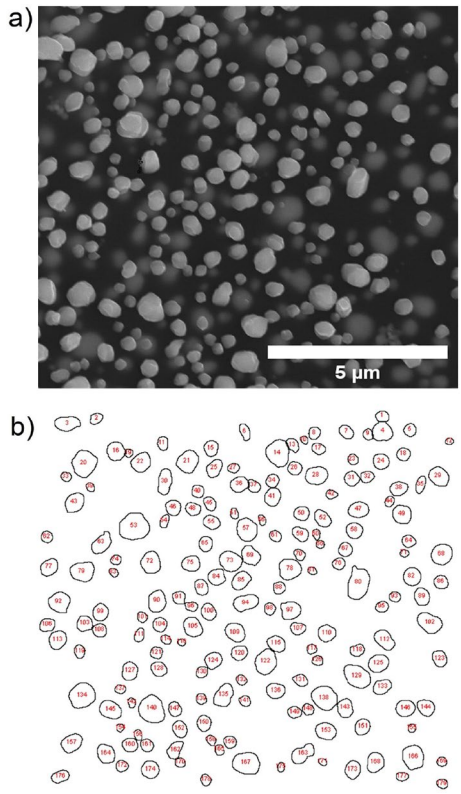


**Figure 6:** Particle size analysis by image processing using Amira and ImageJ. (a) SEM image of particles. (b) Threshold image of particles obtained using ImageJ.

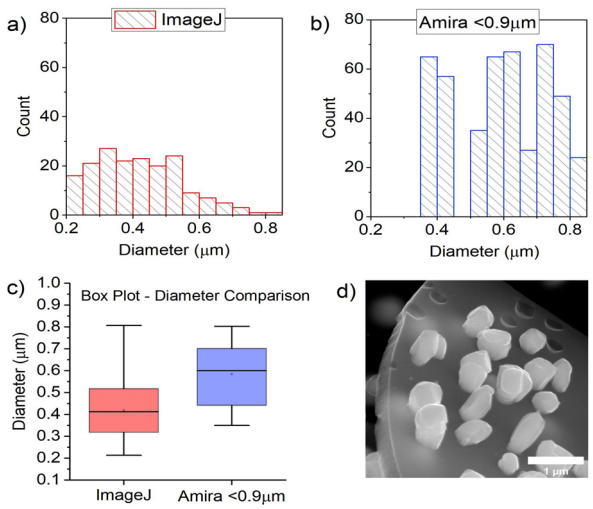


**Figure 7:** Comparison of particle size from Cu-lactose sample by image processing and statistical analysis. Histogram analysis using (a) Amira and (b) ImageJ. (c) A box plot comparison of particle size. (d) SEM image of particles.

into colloids during the mixing step and grow during the annealing step into crystalline particles and may also take in place in Fe, Co, Ni, and Al variations of the carbon foams. These metal cations do form chelate complexes with dissolved sugars [38–40] which may help in the reduction of the ion. Thirdly, these same aqueous metal-sugar ligands may survive the initial mixing and polymerization step, forming metal salts during the curing step, and finally in the annealing step, are reduced by $H_2$ gas and nucleate into particles as in the second mechanism suggested.

These mechanisms represent three possible routes by which metal particles are embedded within the porous carbon matrix. Figure 5 shows the relative size of the particles grown from the metal nitrates chosen. Cu and Ag particles are on the order of 1–2 microns in size while also generating rods. Much like Fe, Ni and Co generated nanosized particles in the range of 50-200 nm. The inset of Fig. 9(a) shows a STEM micrograph of a Co nanoparticle approximately 60 nm in diameter surrounded by graphitic carbon structures. Approximate size of Co nanoparticles was determined to be 58 nm in diameter by Scherrer analysis of the Full Width Half Max calculated from XRD plots of Fig. 8 which agrees with the results from the STEM micrographs. Al nitrate also produced smaller sized particles, below 100 nm. Elemental mapping was performed using EDS to show that the distribution of metal within the porous bulk structure is consistent as seen in Fig. 5. Figure 5 also demonstrates the placement of the metal particles is on both the cell wall ligaments and joints of the porous metal–carbon foam.

Particle size analysis was conducted on the Cu-lactose micro-CT sample from Fig. 4(c) by image processing using two software methods, Amira and ImageJ, and compared. ImageJ was used to threshold the SEM micrograph from Fig. 6(a) to produce Fig. 6(b). Particles with circularity > 0.7 were counted and diameters calculated producing the histogram in Fig. 7(a). No particles with diameter > 0.9 µm were observed using ImageJ. We use this diameter as the upper limit of diameters calculated by Amira. Because of the resolution limitation (0.351 µm voxel size), volumes calculated from Amira included large agglomerations like those seen in Fig. 4(d). Therefore, the 0.9 µm limit observed by ImageJ was used to produce the histogram in Fig. 7(b). Box plots are shown to demonstrate the sample distribution in Fig. 7(c) and the SEM micrograph in Fig. 7(d) also agree with results found from ImageJ and Amira.

### Crystallinity of metal particles

When XRD analysis was conducted graphite was only detected in the Fe, Ni, and Co foams as seen in Fig. 8, which clearly notes the presence of the 27° diffraction peak for graphite producing a Metal Graphite Foam (MGF). The broadness of the peaks may signify the graphite is turbostratic in nature. This is also corroborated with Raman Spectra in Fig. 8 and Electron Energy Loss Spectroscopy (EELS) in Fig. 9. Cu, Ag, and Al did not grow graphite sheets, instead forming metal carbon foams.

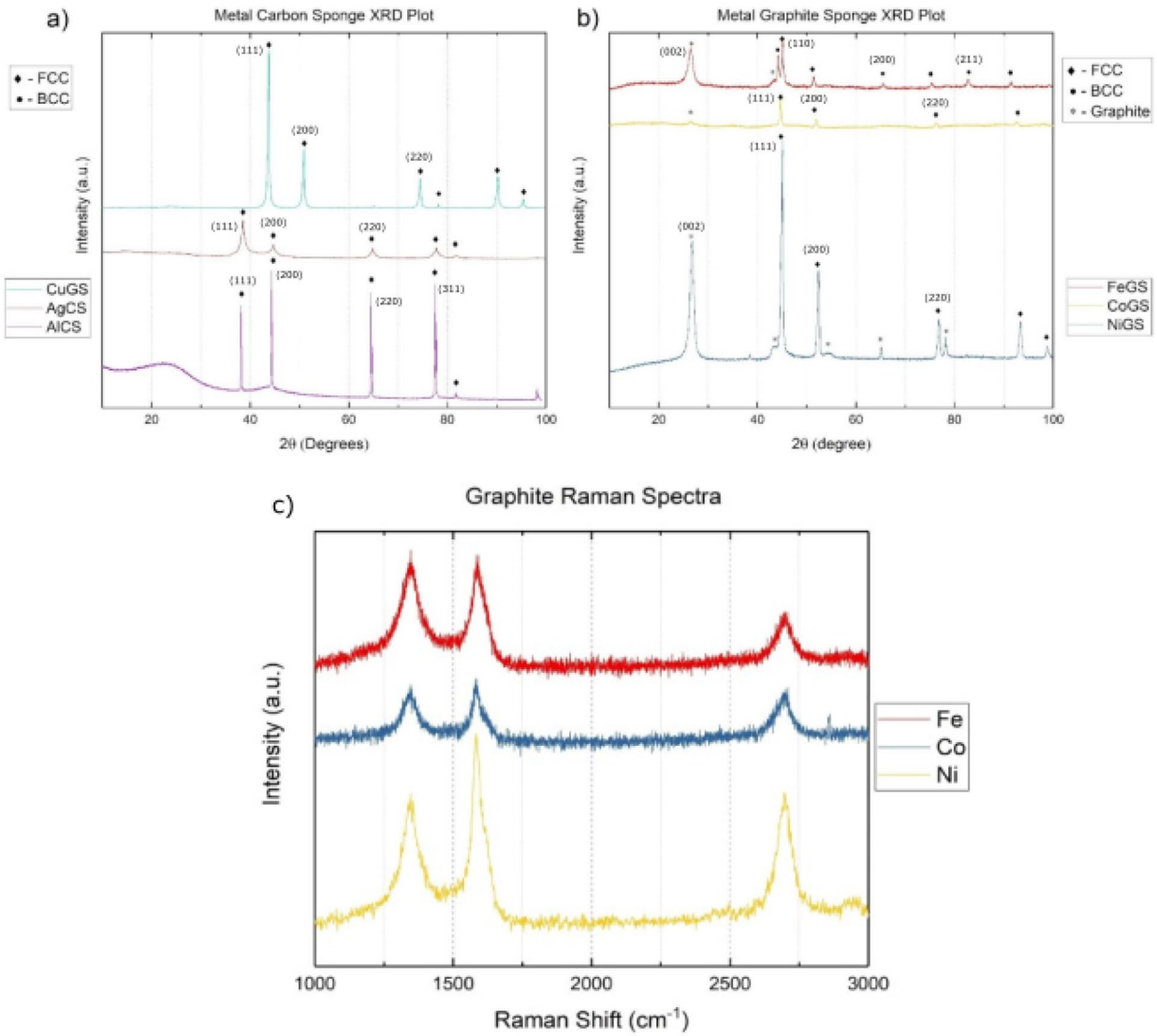


**Figure 8:** XRD Comparison: XRD Spectra showing the presence of (a) crystalline Cu, Ag, and Al particles, (b) crystalline Fe, Co, and Ni particles as well as graphite, and (c) Raman Comparison: Raman Spectra confirming the presence of graphite encapsulating layers in FeGF, CoGF, and NiGF.

Due to this distinction, the resulting materials will be referred to as follows: FeGF, CoGF, NiGF, and CuCF, AgCF, AlCF, respectively. The XRD reflections for each respective metal particles were detected: XRD spectra of FeGF displayed both $\alpha$-Fe and $\gamma$-Fe particles and possibly $Fe_3C$. NiGF and CoGF spectra displayed $\gamma$-Ni and $\gamma$-Co peaks, respectively. CuCF, AgCF, and AlCF each displayed FCC reflections. AgCF also detected a small BCC peak. Nitric acid and sugar controls did not produce graphitic peaks during XRD analysis suggesting that metals are requisite to their growth, but only certain transition metals and localized around those same metal particles as seen in the inset of Fig. 9. XRD measurements and characterization were taken using a PANalytical Empyrean Series 2 copper $k_\alpha$ source X-ray diffractometer. XRD Analysis was performed using ICDD (International Centre for Diffraction Data) database information.

## Developing an insight into the mechanism of graphitic encapsulation

Given the nature of the constituents and temperature at which the metal carbon foams are annealed, comparisons can be made to the growth mechanism of Carbon Nanotubes (CNTs) using catalytic metal nanoparticles, usually Fe, Ni, and Co, by Chemical Vapor Deposition (CVD). Cementite ($Fe_3C$) has also been shown to exhibit catalytic properties, but the work of Wirth et al. suggests that cementite may only be a subset of more complex kinetics and observations during their experiments suggest that

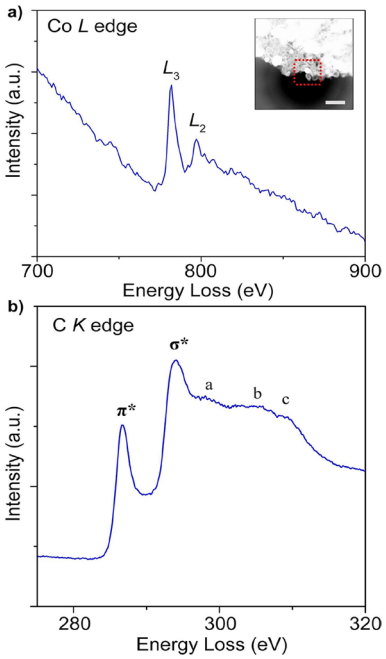


**Figure 9:** (a) EELS cobalt $L_{23}$ edge measured in the region highlighted by the dotted box in the inset STEM micrograph. The STEM micrograph is acquired from a sample of CoGF and shows a Co nanoparticle surrounded by graphitic structures. Scale bar is 200 nm. (b) EELS carbon *K* edge with the characteristic peaks denoted. Fine structure peaks shown in a, b, and c are consistent with EELS of graphitic carbon [32].

cementite is not a prerequisite for growth [41]. The growth of CNTs can be accomplished by CVD synthesis, which is processed at a similar temperature range (625–900 °C), and flow of carbon feedstock gases such as ethylene [42] or methane [43]. There are several differences however; during the annealing process orders of magnitude more carbon is present as a gelatinous resin. Additionally, catalytic metal particles are already present at the start of CNT growth by CVD synthesis; during the annealing of the MGF the metal particles nucleate and grow from the metal atoms or oxides present in the resin, though there are CVD methods that form particles in situ from precursors such as ferrocene [43–45]. Even with these differences, many crystal growth processes and temperatures agree with the XRD data from Hamed and associates [8].

## Metal–carbon phase diagrams

In any case, the particle catalyzing the eutectoid reaction is crystalline and Fe, Co, and Ni are common catalysts for CNT growth because of their ability to decompose carbon feedstocks [28, 45–47]. Successful CNT catalysts are those with high carbon solubility and those which are unsuccessful "typically fall into two categories: either there is no significant solubility of carbon in the metal or numerous stable carbides formed at higher carbon concentrations" [28]. Since no carbides were detected by XRD as seen

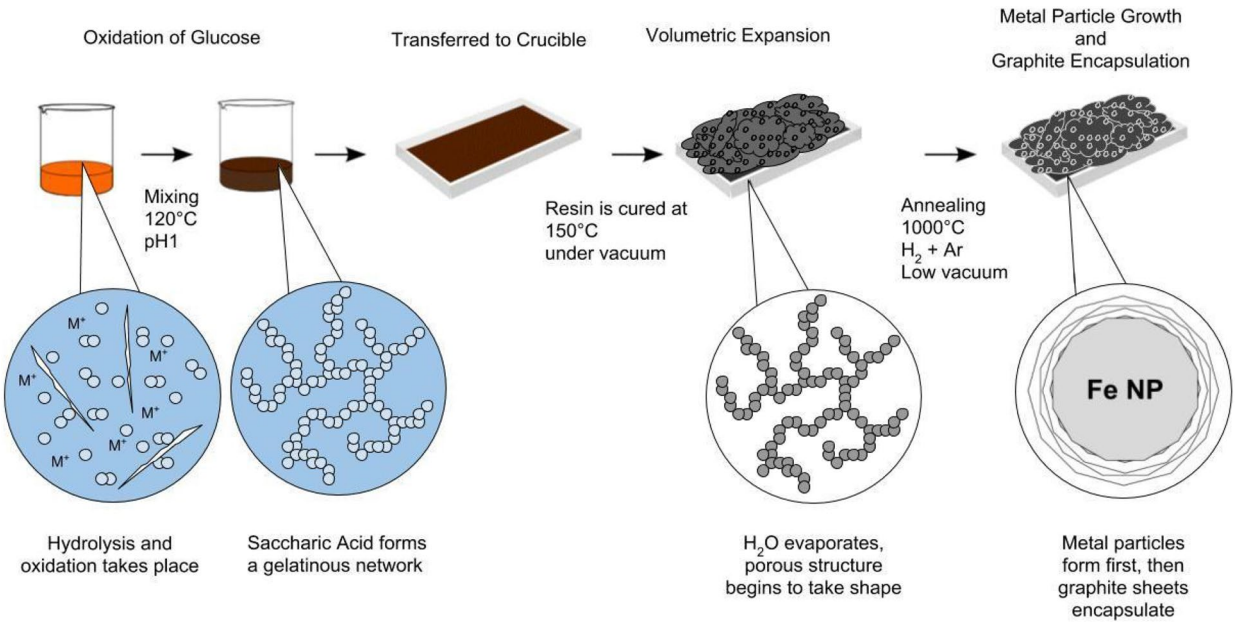


**Figure 10:** Schematic: Precursors undergo hydrolysis and oxidation of saccharides takes place, then gases evaporate causing volumetric expansion and the bulk morphology forms, and the annealing Step where metal particles nucleate and graphitic layers encapsulate some metal nanoparticles.

in Fig. 4, the limited solubility of carbon in the Cu, Ag, and Al solid phases may prevent the dissolution of carbon feedstock into the metal particles and further prevent the nucleation of graphite in the MCFs. In CVD growth the carbon feedstock (acetylene, methane) is in such low concentration that CNTs form and it is only at the end of CNT growth that graphitic encapsulation is observed.

During the annealing step, gelatinous carbon feedstock is present in excess throughout the growth of metal particles (600 °C) and graphite phase separation (700 °C) as verified by XRD [8]. This excess carbon present at the 600–700 °C range may prematurely catalyze graphite formation as metal particles are growing, encapsulating the particle and thus restricting it's growth and size. This may explain why the metals commonly used in CNT synthesis (Fe, Ni, Co) typically display smaller particles sizes than those that do not (Ag, Cu) as seen in Figs. 9 and 5, respectively, Al being the exception. The presence of excess carbon may also prevent CNT synthesis simply due to limited space within the gelatinous matrix suggesting graphite is more likely to precipitate.

## Conclusion

The oxidation of sugar precursors via nitric acid demonstrated a mechanism of polymerization to generate the bulk morphology of a super porous carbon foam. Control experiments conducted with sucrose, glucose, fructose and gluconic acid were investigated to demonstrate the proposed hydrolysis, oxidation, and esterification mechanisms. The viability of varied metal nitrate precursors illustrates the modularity of the synthesis mechanism and its potential to embed metal particles of various sizes and shapes into the bulk morphology of the carbon foam. Characterization via SEM and STEM demonstrated consistency of the bulk morphology of the resulting porous carbon foam and metal particles after oxidation, curing, and annealing between metal nitrate precursors. The distribution of metal particles throughout the bulk structure is shown by EDS, while XRD demonstrates the crystallinity of the particles. Ni and Co particles nucleated graphitic encapsulating layers (detected by XRD, Raman, and EELS) similar to Fe while Ag, Cu, and Al foams did not. Investigation into this disparity lead to a comparison of the growth of graphitic encapsulating layers to the growth of CNTs and is supported by the literature. These findings lay the groundwork to design customizable porous carbon scaffolds with the ability to embed metal particles and implant those same metal's properties into the bulk material. These composite porous materials can be used in future applications toward electrochemical supercapacitors, oil sorption, spill recovery, and bactericidal coatings.

### Synthesis method

#### New metal carbon foams

MCFs were produced utilizing a three-step process using the sucrose, polyvinyl alcohol (PVA), and metal nitrate system as a model from Hamed et al. [8] and is illustrated in Fig. 10. Other nitrate compounds were inspected which might produce metal particles embedded in graphite sheets. The metal nitrates chosen for synthesis were: $Cu(NO_3)_2$, $Co(NO_3)_2$, $Ni(NO_3)_2$, $AgNO_3$, and $Al(NO_3)_3$. Since the difference in oxidation states determines the number of nitrate groups bonded to the cation, each metal nitrate resulted in a different pH in aqueous solution and therefore each was treated with additional nitric acid to ensure a pH of 1 was consistent for each experiment. Sucrose and PVA molar ratios were kept consistent between experiments as well as the annealing temperature. After being annealed in a reducing atmosphere, each formed a metal carbon foam with embedded metal particles, some greater than 100 nm in diameter (Cu, Ag) and some smaller (Co, Ni, Al), though not all developed a graphite encapsulation around the embedded metal particles (Cu, Ag, Al).

#### Agreement with atomistic computations

Molecular Dynamics (MD) computations have been used to model the mechanism and predict the temperatures at which CNTs grow from transition metal nanoparticles [27]. The XRD data from Hamed et al. displays α-Fe peaks at 600 °C and at 700 °C graphite peaks are observed, meaning that at some point between 600 °C and 700 °C, graphite encapsulation begins. This agrees with the results presented in Feng et al. At some point during annealing of the gelatinous resin the graphite growth ends; this could be a point at which carbon has supersaturated the particle and lowered the enthalpy enough to end the phase separation [28, 48, 49].

## Acknowledgments

The authors gratefully acknowledge financial support from the STARnet C-SPIN (Center for Spintronic Materials, Interfaces, and Novel Architectures), sponsored by MARCO and DARPA (Award Number A003571404), Vantage Advanced Technologies LLC (Award Number 16040361), and International Chemical Systems, Inc. (Award Number 21020255). Electron microscopy analysis was carried out in the Characterization Facility of the University of Minnesota, which receives partial support from the NSF MRSEC program (Award Number DMR-2011401). The authors would also like to thank Dr Eric Bushong for his guidance on micro-CT data collection and image reconstruction at the National Center for Microscopy and Imaging at the University of California San Diego.

## Data availability

All data generated and analyzed during this study are included in this article.

## Declarations

**Conflict of interest** All authors declare that they have no conflicts of interest.

## References


1. F. Béguin, V. Presser, A. Balducci, E. Frackowiak, Carbons and electrolytes for advanced supercapacitors. Adv. Mater. **26**, 2219–2251 (2014). https://doi.org/10.1002/adma.201304137
2. C. Wang, M.J. O'Connell, C.K. Chan, Facile one-pot synthesis of highly porous carbon foams for high-performance supercapacitors using template-free direct pyrolysis. ACS Appl. Mater. Interfaces **7**, 8952–8960 (2015). https://doi.org/10.1021/acsami.5b02453
3. Y. Wen, K. He, Y. Zhu, F. Han, Y. Xu, I. Matsuda, Y. Ishii, J. Cumings, C. Wang, Expanded graphite as superior anode for sodium-ion batteries. Nat. Commun. **5**, 1–10 (2014). https://doi.org/10.1038/ncomms5033
4. X. Wang, Y. Zhang, C. Zhi, X. Wang, D. Tang, Y. Xu, Q. Weng, X. Jiang, M. Mitome, D. Golberg, Y. Bando, Three-dimensional strutted graphene grown by substrate-free sugar blowing for high-power-density supercapacitors. Nat. Commun. (2013). https://doi.org/10.1038/ncomms3905
5. R.K. Paul, M. Ghazinejad, M. Penchev, J. Lin, M. Ozkan, C.S. Ozkan, Synthesis of a pillared graphene nanostructure: a counterpart of three-dimensional carbon architectures. Small **6**, 2309–2313 (2010). https://doi.org/10.1002/smll.201000525
6. M. Inagaki, F. Kang, M. Toyoda, H. Konno, *Advanced Materials Science and Engineering of Carbon* (Springer, New York, 2013)
7. J. Ji, L.L. Zhang, H. Ji, Y. Li, X. Zhao, X. Bai, X. Fan, F. Zhang, R.S. Ruoff, Nanoporous Ni(OH)2 thin film on 3d ultrathin-graphite foam for asymmetric supercapacitor. ACS Nano **7**, 6237–6243 (2013). https://doi.org/10.1021/nn4021955
8. H.H. Bay, D. Patino, Z. Mutlu, P. Romero, M. Ozkan, C.S. Ozkan, Scalable multifunctional ultra-thin graphite sponge: free-standing, superporous, superhydrophobic, oleophilic architecture with ferromagnetic properties for environmental cleaning. Sci. Rep. **6**, 1–9 (2016). https://doi.org/10.1038/srep21858
9. H. Bi, X. Xie, K. Yin, Y. Zhou, S. Wan, L. He, F. Xu, F. Banhart, L. Sun, R.S. Ruoff, Spongy graphene as a highly efficient and recyclable sorbent for oils and organic solvents. Adv. Funct. Mater. **22**, 4421–4425 (2012). https://doi.org/10.1002/adfm.201200888
10. H. Bi, Z. Yin, X. Cao, X. Xie, C. Tan, X. Huang, B. Chen, F. Chen, Q. Yang, X. Bu, X. Lu, L. Sun, H. Zhang, Carbon fiber aerogel made from raw cotton: a novel, efficient and recyclable sorbent for oils and organic solvents. Adv. Mater. **25**, 5916–5921 (2013). https://doi.org/10.1002/adma.201302435
11. M. Toyoda, M. Inagaki, Sorption and recovery of heavy oils by using exfoliated graphite. Spill Sci. Technol. Bull. **8**, 467–474 (2003). https://doi.org/10.1016/S1353-2561(03)00131-2
12. M. Toyoda, M. Inagaki, Heavy oil sorption using exfoliated graphite. Carbon N. Y. **38**, 199–210 (2000). https://doi.org/10.1016/s0008-6223(99)00174-8
13. C.H. Lee, N. Johnson, J. Drelich, Y.K. Yap, The performance of superhydrophobic and superoleophilic carbon nanotube meshes in water-oil filtration. Carbon N. Y. **49**, 669–676 (2011). https://doi.org/10.1016/j.carbon.2010.10.016
14. M. Inagaki, H. Nonno, M. Toyoda, K. Moriya, Sorption and recovery of heavy oils by using exfoliated graphite Part I: maximum sorption capacity. Desalination **128**(3), 205–211 (2000)
15. B. Duan, H. Gao, M. He, L. Zhang, Hydrophobic modification on surface of chitin sponges for highly effective separation of oil. ACS Appl. Mater. Interfaces **6**, 19933–19942 (2014). https://doi.org/10.1021/am505414y
16. Q. Zhu, Q. Pan, F. Liu, Facile removal and collection of oils from water surfaces through superhydrophobic and superoleophilic sponges. J. Phys. Chem. C **115**, 17464–17470 (2011). https://doi.org/10.1021/jp2043027
17. N. Brun, C.A. García-González, I. Smirnova, M.M. Titirici, Hydrothermal synthesis of highly porous carbon monoliths from carbohydrates and phloroglucinol. RSC Adv. **3**, 17088–17096 (2013). https://doi.org/10.1039/c3ra41419a
18. M. Inagaki, J. Qiu, Q. Guo, Carbon foam: preparation and application. Carbon N. Y. **87**, 128–152 (2015). https://doi.org/10.1016/j.carbon.2015.02.021
19. N. Frese, S. Taylor Mitchell, A. Bowers, A. Gölzhäuser, K. Sattler, Diamond-like carbon nanofoam from low-temperature hydrothermal carbonization of a sucrose/naphthalene precursor solution. C **3**, 23 (2017). https://doi.org/10.3390/c3030023
20. A. Panáček, L. Kvítek, R. Prucek, M. Kolář, R. Večeřová, N. Pizúrová, V.K. Sharma, T. Nevěčná, R. Zbořil, Silver colloid nanoparticles: synthesis, characterization, and their antibacterial activity. J. Phys. Chem. B **110**, 16248–16253 (2006). https://doi.org/10.1021/jp063826h
21. W.R. Li, X.B. Xie, Q.S. Shi, H.Y. Zeng, Y.S. Ou-Yang, Y. BenChen, Antibacterial activity and mechanism of silver nanoparticles on Escherichia coli. Appl. Microbiol. Biotechnol. **85**, 1115–1122 (2010). https://doi.org/10.1007/s00253-009-2159-5
22. K. Dědková, B. Janíková, K. Matějová, K. Čabanová, R. Váňa, A. Kalup, M. Hundáková, J. Kukutschová, ZnO/graphite composites and its antibacterial activity at different conditions. J. Photochem. Photobiol. B **151**, 256–263 (2015). https://doi.org/10.1016/j.jphotobiol.2015.08.017
23. J.C. Medina, V.I. Garcia-Perez, R. Zanella, Metallic composites based on Ag, Cu, Au and Ag–Cu nanoparticles with distinctive bactericidal effect on varied species. Mater. Today Commun. **26**, 102182 (2021). https://doi.org/10.1016/j.mtcomm.2021.102182
24. N.L.V. Carreño, M.T. Escote, A. Valentini, L. McCafferty, V. Stolojan, M. Beliatis, C.A. Mills, R. Rhodes, C.T.G. Smith, S.R.P. Silva, Adsorbent 2D and 3D carbon matrices with protected

magnetic iron nanoparticles. Nanoscale **7**, 17441–17449 (2015). https://doi.org/10.1039/c5nr04499e

25. E. Piperopoulos, L. Calabrese, A. Khaskhoussi, E. Proverbio, C. Milone, Thermo-physical characterization of carbon nanotube composite foam for oil recovery applications. Nanomaterials (2020). https://doi.org/10.3390/nano10010086
26. B. Singh, S. Kumar, B. Kishore, T.N. Narayanan, Magnetic scaffolds in oil spill applications. Environ. Sci. Water Res. Technol. **6**, 436–463 (2020). https://doi.org/10.1039/c9ew00697d
27. C.L. Mehltretter, C.E. Rist, Sugar oxidation, saccharic and oxalic acids by the nitric acid oxidation of dextrose. J. Agric. Food Chem. **1**, 779–783 (1953). https://doi.org/10.1021/jf60012a005
28. R. Neuman, Carbohydrates from organic chemistry in organic chemistry. Chemistry **13**(31), 8648–8659 (1999)
29. T.N. Smith, K. Hash, C.L. Davey, H. Mills, H. Williams, D.E. Kiely, Modifications in the nitric acid oxidation of D-glucose. Carbohydr. Res. **350**, 6–13 (2012). https://doi.org/10.1016/j.carres.2011.12.024
30. H. Xi, Z. Gao, J. Wang, Kinetics of oxidative decarboxylation of 3,4-methylenedioxymandelic acid to piperonal with dilute nitric acid. Ind. Eng. Chem. Res. **48**, 10425–10430 (2009). https://doi.org/10.1021/ie900961r
31. J. Livage, M. Henry, C. Sanchez, Sol-gel chemistry of transition metal oxides. Prog. Solid State Chem. **18**, 259–341 (1988). https://doi.org/10.1016/0079-6786(88)90005-2
32. C.C. Addison, Dinitrogen tetroxide, nitric acid, and their mixtures as media for inorganic reactions. Chem. Rev. **80**, 21–39 (1980). https://doi.org/10.1021/cr60323a002
33. J. Mu, D.D. Perlmutter, Thermal decomposition of metal nitrates and their hydrates. Thermochim. Acta. **56**, 253–260 (1982). https://doi.org/10.1016/0040-6031(82)87033-0
34. K. Lu, Porous and high surface area silicon oxycarbide-based materials - A review. Mater. Sci. Eng. R Rep. **97**, 23–49 (2015). https://doi.org/10.1016/j.mser.2015.09.001
35. E. Aram, S. Mehdipour-Ataei, A review on the micro- and nanoporous polymeric foams: preparation and properties. Int. J. Polym. Mater. Polym. Biomater. **65**, 358–375 (2016). https://doi.org/10.1080/00914037.2015.1129948
36. S. Panigrahi, S. Kundu, S.K. Ghosh, S. Nath, T. Pal, General method of synthesis for metal nanoparticles. J. Nanoparticle Res. **6**, 411–414 (2004). https://doi.org/10.1007/s11051-004-6575-2
37. S.K. Mehta, S. Chaudhary, M. Gradzielski, Time dependence of nucleation and growth of silver nanoparticles generated by sugar reduction in micellar media. J. Colloid Interface Sci. **343**, 447–453 (2010). https://doi.org/10.1016/j.jcis.2009.11.053
38. B. Gyurcsik, L. Nagy, Carbohydrates as ligands: Coordination equilibria and structure of the metal complexes. Coord. Chem. Rev. **203**, 81–149 (2000). https://doi.org/10.1016/S0010-8545(99)00183-6
39. C.T. Wirth, B.C. Bayer, A.D. Gamalski, S. Esconjauregui, R.S. Weatherup, C. Ducati, C. Baehtz, J. Robertson, S. Hofmann, The phase of iron catalyst nanoparticles during carbon nanotube growth. Chem. Mater. **24**, 4633–4640 (2012). https://doi.org/10.1021/cm301402g
40. P.J. Charley, B. Sarkar, C.F. Stitt, P. Saltman, Chelation of iron by sugars. BBA - Biochim. Biophys. Acta. **69**, 313–321 (1963). https://doi.org/10.1016/0006-3002(63)91264-2
41. H. Zhu, K. Suenaga, A. Hashimoto, K. Urita, K. Hata, S. Iijima, Atomic-resolution imaging of the nucleation points of single-walled carbon nanotubes. Small **1**, 1180–1183 (2005). https://doi.org/10.1002/smll.200500200
42. Y. Homma, Y. Kobayashi, T. Ogino, D. Takagi, R. Ito, Y.J. Jung, P.M. Ajayan, Role of transition metal catalysts in single-walled carbon nanotube growth in chemical vapor deposition. J. Phys. Chem. B **107**, 12161–12164 (2003). https://doi.org/10.1021/jp0353845
43. N. Sano, H. Akazawa, T. Kikuchi, T. Kanki, Separated synthesis of iron-included carbon nanocapsules and nanotubes by pyrolysis of ferrocene in pure hydrogen. Carbon N. Y. **41**, 2159–2162 (2003). https://doi.org/10.1016/S0008-6223(03)00215-X
44. C.P. Deck, K. Vecchio, Prediction of carbon nanotube growth success by the analysis of carbon-catalyst binary phase diagrams. Carbon N. Y. **44**, 267–275 (2006). https://doi.org/10.1016/j.carbon.2005.07.023
45. K.A. Mkhoyan, A.W. Contryman, J. Silcox, D.A. Stewart, G. Eda, C. Mattevi, S. Miller, M. Chhowalla, Atomic and electronic structure of graphene-oxide. Nano Lett. **9**, 1058–1063 (2009). https://doi.org/10.1021/nl8034256
46. F. Ding, P. Larsson, J.A. Larsson, R. Ahuja, H. Duan, A. Rosen, K. Bolton, The importance of strong carbon-metal adhesion for catalytic nucleation of single-walled carbon nanotubes. Nano Lett. **8**, 463–468 (2008). https://doi.org/10.1021/nl072431m
47. F. Ding, A. Roséna, K. Boltona, Dependence of SWNT growth mechanism on temperature and catalyst particle size: bulk versus surface diffusion. Carbon N. Y. **43**, 1–8 (2005)
48. S. Janssens, G. Van den Mooter, Review: physical chemistry of solid dispersions. J. Pharm. Pharmacol. **61**, 1571–1586 (2009). https://doi.org/10.1211/jpp/61.12.0001
49. F. Ding, K. Bolton, A. Rosén, Nucleation and growth of single-walled carbon nanotubes: a molecular dynamics study. J. Phys. Chem. B **108**, 17369–17377 (2004). https://doi.org/10.1021/jp046645